CONDENSED MATTER PHYSICS

Quantum plasmonic control of trions in a picocavity with monolayer WS_2

Zhe He[1], Zehua Han[1], Jiangtan Yuan[2], Alexander M. Sinyukov[1], Hichem Eleuch[1,3], Chao Niu[4,5], Zhenrong Zhang[4,6], Jun Lou[2], Jonathan Hu[4,5]*, Dmitri V. Voronine[7]*, Marlan O. Scully[1,4]

Monitoring and controlling the neutral and charged excitons (trions) in two-dimensional (2D) materials are essential for the development of high-performance devices. However, nanoscale control is challenging because of diffraction-limited spatial resolution of conventional far-field techniques. Here, we extend the classical tip-enhanced photoluminescence based on tip-substrate nanocavity to quantum regime and demonstrate controlled nano-optical imaging, namely, tip-enhanced quantum plasmonics. In addition to improving the spatial resolution, we use the scanning probe to control the optoelectronic response of monolayer WS_2 by varying the neutral/charged exciton ratio via charge tunneling in Au-Ag picocavity. We observe trion "hot spots" generated by varying the picometer-scale probe-sample distance and show the effects of weak and strong coupling, which depend on the spatial location. Our experimental results are in agreement with simulations and open an unprecedented view of a new range of quantum plasmonic phenomena with 2D materials that will help to design new quantum optoelectronic devices.

INTRODUCTION

Two-dimensional (2D) transition metal dichalcogenides (TMDs) have attracted worldwide attention for their promising applications in photonics (*1*), sensing (*2*), and optoelectronic nanodevices (*3*). Low-dimensional quantum confinement effects play a major role in the optoelectronic response of 2D TMDs such as monolayer tungsten disulfide (WS_2) (*4*). Many-body states such as neutral excitons, trions, and biexcitons govern the photoresponse in TMDs (*5*, *6*). Their interconversion may be controlled by using photoexcitation or bias, which strongly depends on the local inhomogeneities such as impurities, defects, or external dopants. As a result, unlike the bulk materials, the optoelectronic properties of monolayer WS_2 are dominated by excitons and trions (*4*). Therefore, controlling the excitons in 2D TMDs allows the manipulation of the device performance.

Previous work on the control of neutral excitons (X^0) and negatively charged trions (X^-) was based on the exciton interconversion $X^0+e^- \rightarrow X^-$ via gating (*7*), photoexcitation (*8*), plasmonic hot carriers (*9*), and chemical doping (*10*). However, the nanoscale optical control of the 2D materials has not yet been realized. Nanoscale control of trions is of great importance in optoelectronic nanodevices, for example, carbon nanotube film–based electroluminescence devices (*11*) and MoS_2-based field-effect transistors (*12*). Here, we show that quantum plasmonics provides a convenient and effective tool for generation, nanoimaging, and control of trions in 2D materials.

Quantum plasmonics plays an important role when the dimensions of plasmonic nanostructures reach a critical subnanometer size (*13*), as, for example, in the picoscale cavity formed by the plasmonic scanning probe and metal substrate (*14*). Few-layer MoS_2 in the picocavity showed interesting tunneling-induced photoluminescence (PL) and Raman quenching effects (*14*). However, although the classical plasmonic modulation of excitons in MoS_2 has been achieved (*15*, *16*), the quantum yield of exciton generation is low in few-layer compared to monolayer 2D materials, and the quantum plasmonic control of trions in monolayer TMDs was not yet explored. Using tip-enhanced quantum plasmonic (TEQPL) imaging, we show that it is possible to locally control both neutral excitons and trions in monolayer WS_2. Compared to the classical plasmonic imaging, TEQPL can be used to control and monitor the exciton interconversion by varying the size of the picocavity.

The classical tip-enhanced PL (TEPL) technique provides a high spatial resolution beyond the optical diffraction limit due to the near-field (NF) enhancement of the PL signals by localized surface plasmon resonances of a plasmonic scanning probe such as a silver- or gold-coated nanotip (*14*, *17*). The classical tip-substrate coupling leads to the large local electric field enhancement within a tip-sample distance of $1 < d < 10$ nm with an additional enhancement in the case of a metallic substrate via gap-mode plasmons. However, for very small subnanometer gaps, the NF enhancement may be reduced because of the quantum plasmonic effects such as tunneling of surface charges in the gap plasmon TMD system (*14*). As a result, the tunneling electrons reduce the overall surface charges and the corresponding local electromagnetic fields at the probe (*18*, *19*). Previously, we reported similar control experiments in a plasmonic picocavity made of a pure gold substrate and gold tip (without WS_2) and observed quantum plasmonic quenching due to electron tunneling (*14*). Here, we use quantum plasmonic effects in a Au-Ag substrate-tip picocavity to control trions in monolayer WS_2 by the tunneling charges. In addition, because of the picometer-scale control of the tip-sample distance, we obtained picoscale control of the photoresponse in the vertical tip-sample coupling direction. Using TEQPL, we achieved both imaging and control of neutral excitons and trions with a high lateral spatial resolution of ~80 nm. This is the first demonstration of quantum plasmonic interconversion of neutral excitons to trions in 2D materials, which has promising applications for novel nanoscale light-matter interaction schemes in atomically thin semiconductors.

RESULTS

The schematic representation of the experimental setup is shown in Fig. 1A. We used the state-of-the-art commercial scanning probe

[1]Institute for Quantum Science and Engineering, Texas A&M University, College Station, TX 77843, USA. [2]Department of Materials Science and NanoEngineering, Rice University, Houston, TX 77005, USA. [3]Department of Applied Sciences and Mathematics, College of Arts and Sciences, Abu Dhabi University, Abu Dhabi, United Arab Emirates. [4]Baylor Research and Innovation Collaborative, Baylor University, Waco, TX 76798, USA. [5]Department of Electrical and Computer Engineering, Baylor University, Waco, TX 76798, USA. [6]Department of Physics, Baylor University, Waco, TX 76798, USA. [7]Department of Physics, University of South Florida, Tampa, FL 33620, USA.
*Corresponding author. Email: voronine@usf.edu (D.V.V.); jonathan_hu@baylor.edu (J.H.)

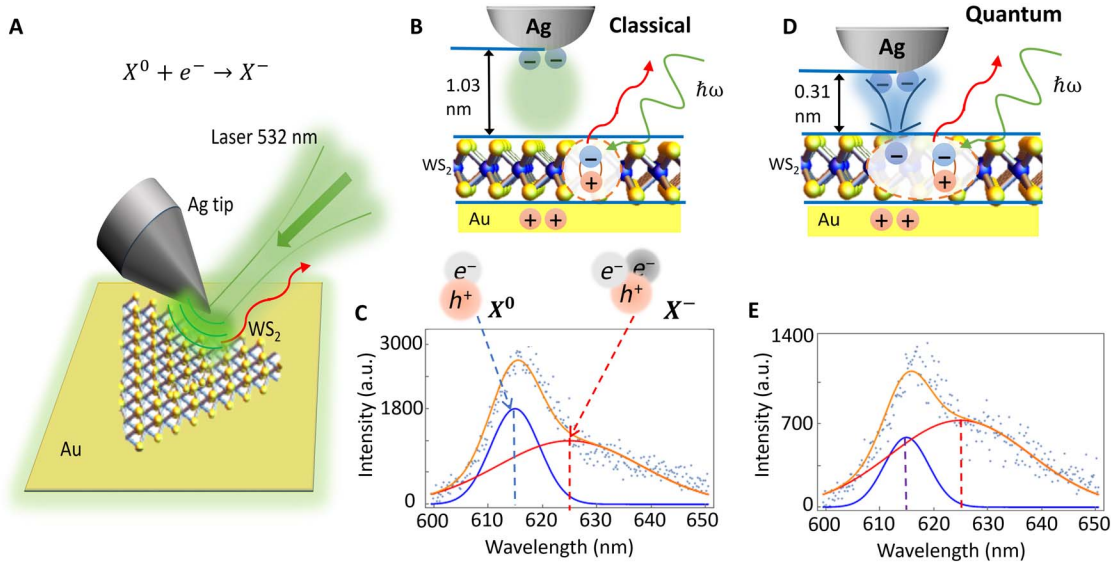

Fig. 1. Quantum plasmonic generation of trions in a Au-Ag picocavity with monolayer WS_2. (**A**) Schematic of TEQPL imaging with monolayer WS_2 in a picocavity formed by the Ag tip and the Au substrate. The 532-nm laser beam was focused on the tip apex, and the sample was scanned to obtain the PL spatial maps of neutral excitons (X^0) and trions (X^-). The tunneling-induced $X^0 \rightarrow X^-$ transition takes place for the short tip-sample distance. (**B**) Sketch of the Au-Ag cavity with $d > 1$ nm tip-sample distance that corresponds to the classical coupling (CC) regime. (**C**) PL spectra of X^0 and X^- in monolayer WS_2 in the CC regime. Blue and red solid lines are Gaussian fitting functions centered at 614 and 625 nm, respectively. a.u., arbitrary units. (**D** and **E**) Corresponding sketch and PL spectra of monolayer WS_2 in the Au-Ag picocavity in the quantum coupling (QC) regime with a tip-sample distance $d < 0.35$ nm, where the charge tunneling [blue arrow in (D)] contributes to the formation of trions. The PL intensity of X^- becomes larger than that of X^0 in the QC (E) compared to the CC (C) regime.

microscopy system to perform the coupled atomic force microscopy (AFM) and nano-optical TEQPL experiments with precisely controlled tip-sample distance (OmegaScope-R coupled with LabRAM, HORIBA Scientific; details are given in Materials and Methods). Au-coated Ag tip was mounted on an AFM cantilever, and the 532-nm laser was focused on the tip apex, leading to the enhancement of local electric fields in the tip-substrate cavity. To study the quantum plasmonic effects, we constructed a picometer-gap cavity between the Au substrate and the Au-coated Ag tip by calibrating the tip-sample distance using the force-distance analysis, which was previously described (*14*) and is shown in fig. S1. Briefly, we used the short-distance approximation of the Lennard-Jones potential to estimate the tip-sample distance within the van der Waals (vdW) contact between the Au and S atoms (0.35 nm) (*20*). We used the vdW radii of 0.166 nm (Au) and 0.180 nm (S) for the estimation of the 0.346-nm Au-S contact.

Figure 1 (C and E) shows the PL spectra of monolayer WS_2 in the Au-Ag cavity fitted by two Gaussian functions (*19*) centered at the PL signals of X^0 (614 nm) and X^- (625 nm). Similar observations of trionic emission on both nonmetallic (*4*, *10*, *21*, *22*) and metallic (*23*–*26*) substrates show negative trion peaks at room temperature. Figure S10 shows the corresponding PL signals of WS_2 on the Si/SiO_2 substrate as compared with the PL signals on the Au substrate. The PL spectra on the Si/SiO_2 substrate are in agreement with previous reports (*21*, *27*) and show similar line shapes with ~30-meV separation between the PL peaks of neutral excitons and trions, indicating similar values of the binding energies on both substrates. The relative blue shift of ~10 nm on the Au substrate compared to the Si/SiO_2 substrate may be due to the combination of surface plasmonic effects (*10*, *21*, *28*), and the release of strain in chemical vapor deposition (CVD)–grown WS_2 may be due to the transfer on Au (*25*, *26*).

Several previous theoretical studies predicted a strong dependence of the binding energy of both neutral excitons and trions on the dielectric properties of the substrate (*29*–*31*), which was confirmed experimentally for neutral excitons; however, contrary to the predictions, only a weak dependence of binding energy on the substrate was shown experimentally for trions (*32*, *33*). Another recent model accounted for this difference by treating the monolayer TMD behavior of the transition metal and chalcogenide atomic sheets (*34*). The trion wave functions, confined to the middle layer transition metal sheet, were screened by the outer chalcogen layers. In addition, the model included the polaron effects of lattice distortion due to the charged exciton, which increased the effective mass of the trion and increased the trion's binding energy. This weak dependence allowed the observation and control of trions on metallic substrates at room temperature.

Panels C and E of Fig. 1 correspond to the two representative tip-sample distances d for the classical coupling (CC) and quantum coupling (QC) regimes with $d > d_0$ and $d < d_0$, shown in Fig. 1 (B and D, respectively), where $d_0 = 0.35$ nm is the vdW contact distance. When $d = 0.31$ nm (QC; Fig. 1E), the peak ratio of the X^- and X^0 signals is larger than that of $d = 1.03$ nm (CC; Fig. 1C), which indicates that the relative ratio of trions to neutral excitons increased because of tunneling.

Quantum plasmonic control of trions in monolayer WS_2 in the Au-Ag cavity was further investigated as a function of the tip-sample distance as shown in Fig. 2. AFM imaging confirmed the monolayer uniform thickness and a high quality of the triangular-shaped WS_2 nanoflake (Fig. 2A). The PL intensity measured in the spatial location marked by a circle in Fig. 2A was investigated as a function of the tip-sample distance in the range of 10 nm down to a few hundred picometers, which correspond to the CC and QC regimes, respectively (Fig. 2C). Figure 2B shows the PL quenching of both neutral excitons (X^0; blue) and trions (X^-; red) at the picoscale distances. The rates of the X^0 and X^- quenching are different due to the different mechanisms such as the tunneling-induced decrease in the local electric field at the tip

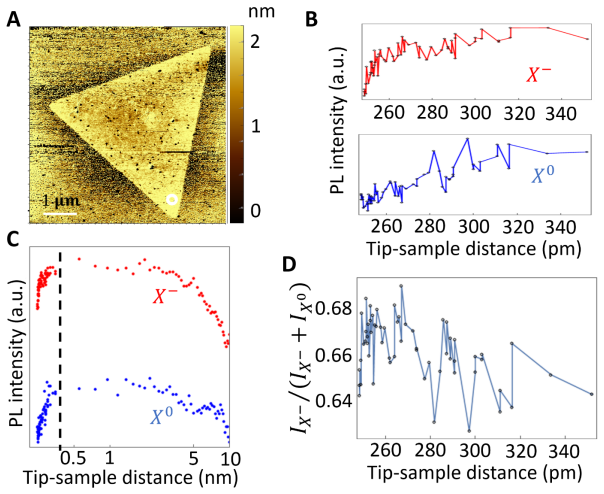

Fig. 2. Picoscale quantum plasmonic control of neutral excitons (X^0) and trions (X^-) in monolayer WS_2 in a Au-Ag cavity. (**A**) AFM image of the triangular monolayer WS_2 nanoflake. PL intensity of neutral excitons (X^0; blue) and trions (X^-; red) measured in a spatial location marked by a circle in (A) as a function of the tip-sample distance in the picometer scale (**B**) and in the whole range (**C**) shows the PL quenching of both signals at the picoscale distances. (**D**) However, the ratio $I_{X^-}/(I_{X^0} + I_{X^-})$ shows an increase in the trion relative to the neutral exciton signal at distances shorter than 300 pm.

apex (*14*, *35*, *36*) and the tunneling-assisted exciton-trion interconversion (*12*, *35*). The PL ratio $I_{X^-}/(I_{X^0} + I_{X^-})$ shows an increase in the trion signal at distances shorter than ~300 pm (Fig. 2D). More examples are shown in fig. S2.

We then performed similar measurements on a complex WS_2 nanoflake, which consists of several areas of interest including a monolayer periphery and a few-layer center as well as a multilayer structural defect at the right corner shown by the AFM height variations in Fig. 3A. TEQPL imaging provides a sensitive method for probing the heterogeneity of the nano-optical response of 2D materials. We obtained PL images of neutral excitons and trions by plotting the integrated areas under the corresponding fitted PL spectra (Fig. 3, C to F). We observed differences between the NF (Fig. 3, C and E) and far-field (FF) (Fig. 3, D and F) PL images of the complex WS_2 nanoflake in a Au-Ag cavity with tip-sample distances of 0.31 and 10 nm, respectively. Compared with the FF images, the NF TEQPL images show a higher spatial resolution and reveal a rich variety of features. For example, the width of the Au-WS_2 interface at the edge of the flake was measured as ~82 and 881 nm using the NF and FF X^- PL signals, respectively (Fig. 3G). The AFM profile in Fig. 3G indicates the position of the WS_2-Au substrate boundary, which correlates well with the optically detected boundary in the NF images. The origin of the increased roughness of the AFM height profile in Fig. 3G is the use of the same Au-coated Ag tip for the AFM measurements and the simultaneous TEPL. The metal coating of the tip leads to the enhanced tip-sample interaction, which is responsible for the increased noise level with the estimated SD of the height profile to be less than 1 nm.

Because TEQPL is based on tunneling, it is very sensitive to the thickness of the sample placed in the gap mode–enhanced electric field of the cavity. This leads to a higher imaging contrast of TEQPL compared to the conventional FF PL. For example, the few-layer central triangle part of the WS_2 nanoflake is better resolved in the NF TEQPL images (Fig. 3, C and E) than in the FF PL images (Fig. 3, D and F). In addition, the top (G) and right (I) corners of the WS_2 nanoflake have low intensities in both the FF and NF signals due to the presence of the charge doping effects in G and multilayer structural defects in I. The increase in the height in I is supported by the correlated AFM data in Fig. 3A. The charge doping is supported by the correlated Kelvin probe force microscopy (KPFM) image, which shows the surface contact potential difference (CPD) signal in Fig. 3B. KPFM shows larger signals in the G and I corners compared to H, which anticorrelate with the PL signal intensities. It has been previously shown that charge doping reduces the PL signals in 2D materials, which is in agreement with our results.

The apparent lack of the clear triangular shapes in the FF and NF images is a result of the limited spatial resolution of ~880 and 80 nm for FF and NF, respectively, which limits the ability to resolve small triangular features (especially for the FF) in the chosen relatively small (~4-μm-size) nanoflake. The flake outlines in the NF images in Fig. 3 (C and E) exhibit the triangular shape more clearly than the corresponding FF images in Fig. 3 (D and F). Still, the absence of the full triangular outline is due to two effects, namely, charge doping and multilayer structural defect. In addition to the intrinsic charge doping of the nanoflake, there is also a quantum plasmonic contribution due to the plasmon-induced electron tunneling from the tip to the sample. Therefore, we performed KPFM measurement both without and with the simultaneous laser excitation (fig. S4, A and B, respectively). Now, it is more clearly seen that quantum plasmonic charge doping leads to the notable variation of the CPD across the G to H line of the KPFM image in fig. S4B.

More detailed information about the sample heterogeneity and the correlation of the AFM topography, KPFM surface potential, and PL signals is shown in the line profiles in Fig. 3 (G and H) obtained from the spatial maps, as indicated by white dashed lines (i) and (ii), respectively. The weaker PL signal from the central area is due to the indirect bandgap nature of multilayer WS_2. Both FF PL and NF TEQPL signals are strong when the sample thickness is small, as shown in the line profiles in Fig. 3H. The NF TEQPL signals show a higher spatial resolution and qualitatively new spatial features compared to the FF PL signals. Different areas of strong PL signals ("hot spots") exist at different locations in the NF images. For example, the left corner (H) shows strong FF PL hot spots of both neutral excitons (Fig. 3D) and trions (Fig. 3F). However, these hot spots are suppressed in the corresponding NF images (Fig. 3, C and E). In addition, the FF profiles of neutral excitons and trions are similar (Fig. 3H, green and orange lines), but the corresponding NF profiles show maximum intensity peak shifts of X^0 and X^- (blue and red lines with shifted maxima highlighted by the vertical dashed lines), which indicates a possible quantum plasmonic tip-induced conversion $X^0 \rightarrow X^-$ in certain spatial locations. This qualitative difference between the hot spots in the FF and NF signals indicates the importance of the tip-sample interaction during the imaging, and it can be used for both imaging and controlling the excitons in 2D materials simultaneously by adjusting the appropriate instrument parameters. The PL spectra at different tip-sample distances and the corresponding $I_{X^-}/(I_{X^0} + I_{X^-})$ ratios for different spots labeled A to E in Fig. 3 (A and B) are shown in fig. S2. These selected spots provide a rich picture of various heterogeneous photoresponses. The results were reproducible as shown by the two consecutive distance dependence measurements at spot B in fig. S6. Further insight into the sample heterogeneity may be obtained by a more detailed analysis of the NF TEQPL maps. For example, figs. S7 and S8 show zoomed-in X^0 and X^- maps with anticorrelated subwavelength features. The regions of large intensity in the X^- map in fig. S7B reveal trion hot spots (dashed circles). Similar regions

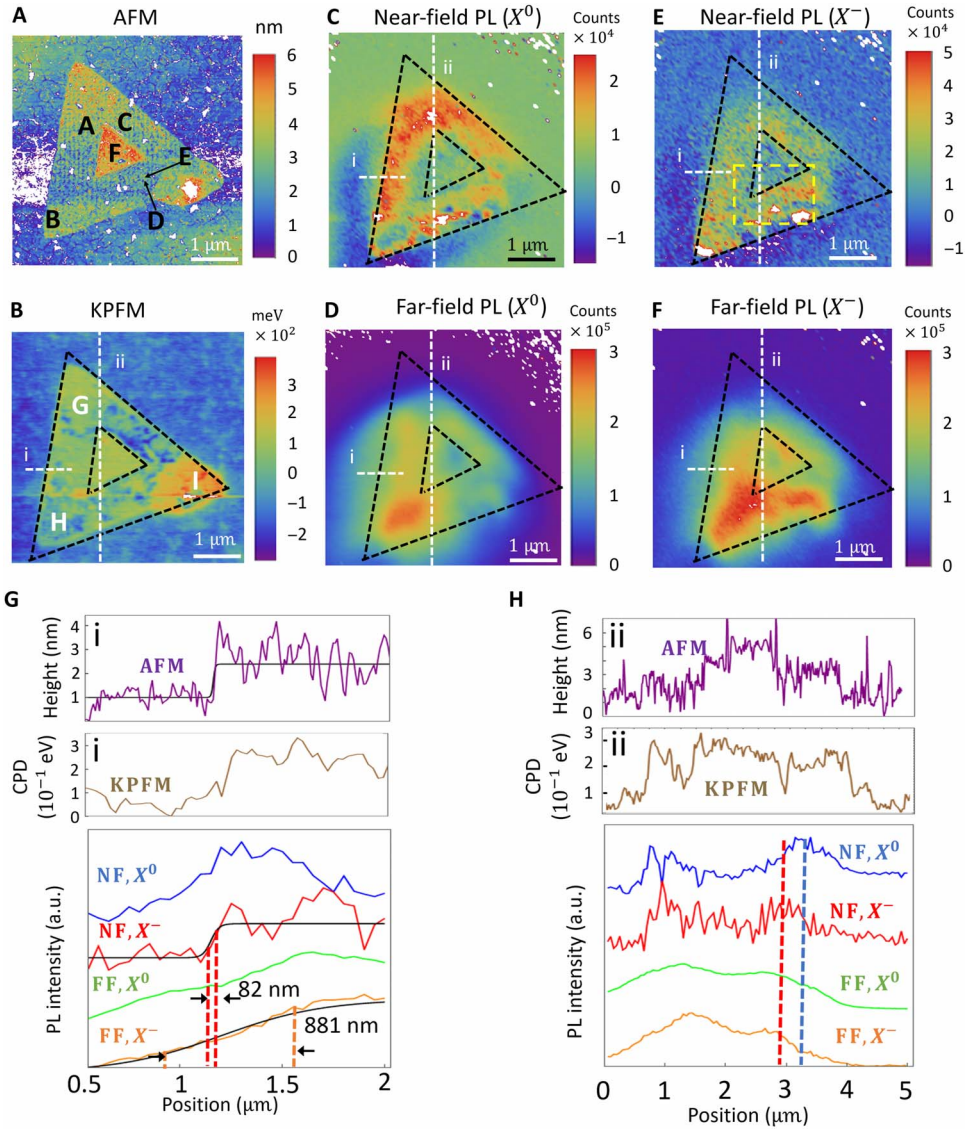

Fig. 3. TEQPL imaging of a complex WS_2 nanoflake. (**A**) AFM image shows the height topography with WS_2 triangular monolayer periphery and a few-layer triangular central region. Several areas of interest are marked A to F in different parts of the flake. (**B**) Kelvin probe force microscopy (KPFM) image under a 532-nm laser illumination shows inhomogeneous contact potential difference (CPD) signal at the surface of the sample. G to I mark the top, left, and right corners, respectively. NF neutral exciton, X^0 (**C**), and trion, X^- (**E**), TEQPL, and FF X^0 (**D**) and X^- (**F**) PL images of the complex WS_2 nanoflake in a Au-Ag cavity with tip-sample distances of 0.31 and 10 nm, respectively. Black dashed lines indicate the outlines of the WS_2 nanoflake. The imaging step size is 50 nm. (**G** and **H**) Line profiles of the AFM, KPFM, and PL signals from the marked white dashed lines (i) and (ii), respectively. Vertical orange and red dashed lines in (G) mark the width of the FF and NF PL profiles, respectively, of trions at the Au-WS_2 interface at the edge of the flake. Vertical blue and red dashed lines in (H) mark the positions of the maximum signal intensities of the NF PL signal profiles of neutral excitons and trions, respectively, showing the relative shift of the two signals.

in the X^0 map show the suppression of the PL signal in fig. S7A. This provides evidence for the $X^0 \rightarrow X^-$ conversion due to the tunneling-induced tip-sample interaction. While FF PL maps show microscale variation of contrast, they do not show any localized anticorrelations (fig. S7, C and D).

The tip-sample distance used for the TEQPL images in Fig. 3 (C and E) corresponds to the QC regime, where the local electric field was partially quenched by tunneling, leading to a large contribution of the $X^0 \rightarrow X^-$ transition. The TEQPL images revealed a highly inhomogeneous pattern with localized regions of strong PL signals (hot spots) in accordance with previous reports of nano-optical imaging of 2D materials (*17*, *37*). Here, we further investigated the tip-sample distance dependence from different spatial locations within the complex WS_2 nanoflake. Figure 4 shows the tip-sample distance dependence of the X^0 and X^- PL signal intensities from two spatial locations marked in Fig. 3A as spot A (Fig. 4, B and C) and spot C (Fig. 4, D and E). These two locations represent the typical examples of strong and weak quantum tip-sample coupling, which correspond to the complete and incomplete quenching of the PL signals in the QC regime. Because of the small size of the tip apex, its influence on the FF PL signals within the 10-nm range can be ignored. Therefore, the effects of the varying tip-sample distance on the FF signals can be ignored, and one expects the same FF contributions to the PL signals at all tip-sample distances plotted in Fig. 4.

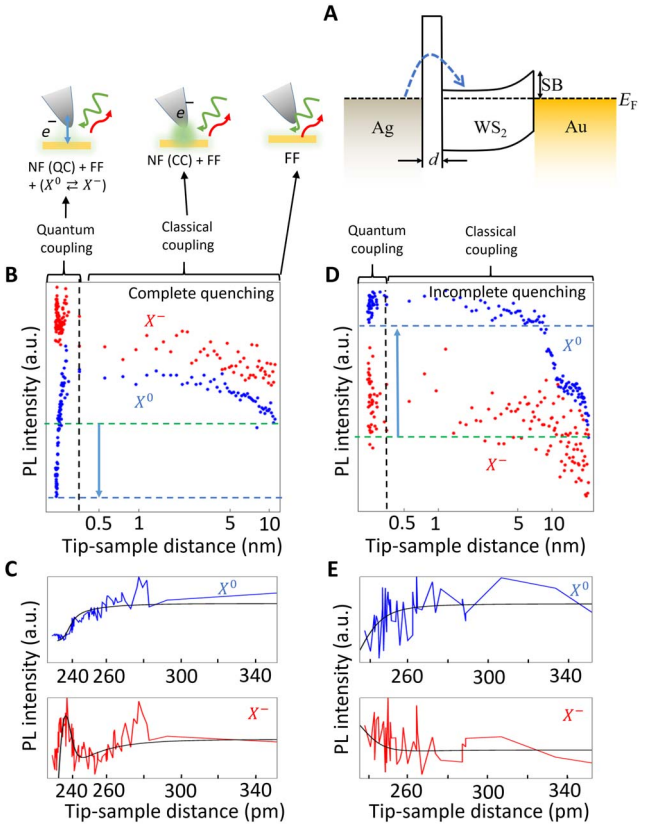

Fig. 4. Tip-sample distance dependence of PL of WS_2 nanoflake in a Au-Ag cavity. (**A**) Energy diagram of the tip-sample-substrate (Ag-WS_2-Au) system with Schottky barrier (SB). Tip-sample distance dependence of the PL signal intensities of neutral excitons (X^0) and trions (X^-) from two spatial locations marked A (**B** and **C**) and C (**D** and **E**) in Fig. 3A. Three regimes of tip-sample coupling are identified in (B): (i) FF with no tip-sample coupling (d > 10 nm), (ii) NF with classical tip-sample coupling (NF CC) with 0.35 nm < d < 10 nm, and (iii) NF with quantum tip-sample coupling (NF QC) with d < 0.35 nm. Green and blue dashed lines indicate the FF and the short-distance NF X^0 PL signals, respectively. Zoomed-in picoscale tip-sample distance dependence of TEQPL signals from spatial locations A (C) and C (E) in the QC regime. The vertical black dashed lines separate the CC and QC regimes at the vdW tip-sample contact distance (0.35 nm).

We consider three different regimes of tip-sample coupling, which are indicated by arrows and corresponding schematic diagrams in Fig. 4B: (i) FF with no tip-sample coupling (with tip-sample distance d > 10 nm and pure FF excitation), (ii) NF with classical tip-sample coupling (NF CC) with tip-sample distance 0.35 nm < d < 10 nm, and (iii) NF with quantum tip-sample coupling (NF QC) with d < 0.35 nm. Case (ii) corresponds to the classical NF coupling, while case (iii) corresponds to the NF coupling with strong quantum plasmonic effects due to field quenching via tunneling and $X^0 \rightarrow X^-$ transition. Figure 4B shows the enhancement and quenching of the X^0 and X^- PL signals in the NF CC and QC regimes, respectively. The X^0 PL intensity at short tip-sample distances of <250 pm is smaller than the X^0 FF PL intensity at a long distance of 10 nm, as indicated by the horizontal blue and green dashed lines in Fig. 4B, respectively. In the absence of the $X^0 \rightarrow X^-$ transition, one would expect the same PL intensities in the case of the complete NF PL quenching at short tip-sample distance as in the case of the long-distance FF PL signal. This is because tunneling completely suppresses the NF enhancement in the QC regime (*14*). In the case of the incomplete PL quenching, the PL intensities at the short tip-sample distances are larger than at the long distances. This is observed in the incomplete quenching case where the NF QC PL (blue dashed line) is larger than the FF PL (green dashed line) in Fig. 4D. However, this is not the case in the complete quenching case where the opposite behavior is observed (Fig. 4B). This may be attributed to the $X^0 \rightarrow X^-$ contribution, which reduced the number of X^0 below the FF limit. This shows the main difference between the classical TEPL imaging technique, where the tip-sample interaction only leads to the confinement of the enhanced electric field. Because of the inhomogeneity of the WS_2 nanoflake under the ambient conditions in air, the Schottky barrier (SB) depends on the local surface energy (*38*), leading to the inhomogeneous local quenching behavior. The incomplete quenching may take place when the electron tunneling is suppressed by the WS_2-gold SB, while in the complete quenching case, the SB is low. In addition, the variations in the local electrostatic environment under the ambient conditions, revealed by the inhomogeneous CPD images in KPFM (Fig. 3B and fig. S4), result in different tip-WS_2 tunneling efficiencies, which, together with SB, determine the PL quenching. The spatial locations in Figs. 2 and 4B showed complete PL quenching, while the spatial locations in Fig. 4D and fig. S3 showed incomplete PL quenching. Only the spots with complete PL quenching showed a substantial decrease in the X^- signals in the QC range of 360 to 260 pm due to the strong contributions of the quantum plasmonic quenching effects needed to support the $X^0 \rightarrow X^-$ conversion.

Here, we show that the tip-sample distance is a convenient control parameter. For example, Fig. 4 (C and E) shows zoomed-in picoscale tip-sample distance dependence of TEQPL signals from spatial locations A and C in Fig. 3A. Figure 4C shows a decrease in the X^- PL signal with a decrease in the tip-sample distance until it reaches ~250 pm. Classically, the opposite trend is expected in which the PL signal increases with the decrease in the gap due to the plasmonic gap-mode enhancement. Therefore, the observed PL quenching is attributed to the tunneling-induced quenching of the plasmonic fields. Similar effects were previously predicted and observed in metallic plasmonic systems (*13*, *14*, *39*). However, after the further decrease in the tip-sample distance below 250 pm, the X^- PL signal increases again with the simultaneous decrease in the X^0 PL signal. This gives strong evidence for the tunneling-induced contribution of the $X^0 \rightarrow X^-$ transition. Then, subsequently, the X^- PL signal decreases again with the further decrease in the tip-sample distance below 240 pm, which is attributed to the formation of the conductive channel in the reduced tip-substrate cavity gap. As a result, all the optical NF signals are suppressed. We developed a theoretical model described in Materials and Methods, which was used to successfully fit the data shown in Fig. 4 (C and E, black lines).

The tip-sample distance dependence plots in Fig. 4 show the overall quenching of the PL signals of neutral excitons in both CC and QC regimes. However, the signals of trions show less changes in the QC regime for the selected spatial locations. The quenching rates for the neutral excitons and trions are different due to the contribution of the $X^0 \rightarrow X^-$ transition. To show more clearly the competition of these two mechanisms, we use the peak ratio $I_{X^-}/(I_{X^0} + I_{X^-})$ from the two adjacent spots that are separated by 60 nm, E (Fig. 5 A and B) and D (Fig. 5 C and D). In the CC regime, these peak ratios are constant and do not depend on the tip-sample distance (see fig. S2). However, in the QC regime, spot E shows a decreasing ratio at d < 260 pm (Fig. 5B), and spot D shows the opposite behavior with an increasing ratio (Fig. 5D). This can be understood by analyzing the behavior of the X^0 and X^- PL signals separately for these two spots. Figure 5C shows that the X^- PL intensity in

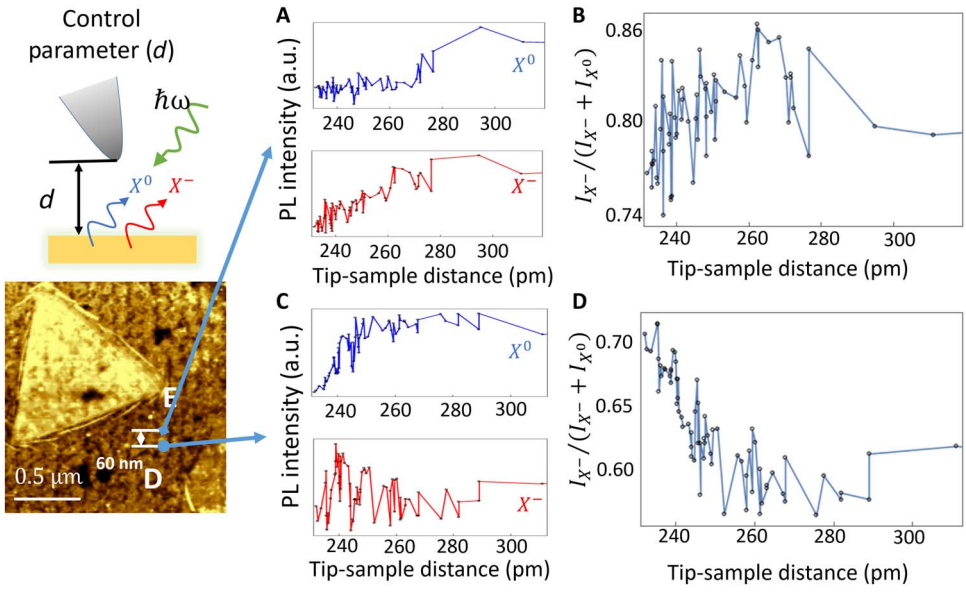

Fig. 5. Subwavelength control of trions in an Au-Ag picocavity with monolayer WS_2. Zoomed-in picoscale tip-sample distance dependence of TEQPL signals of neutral excitons X^0 (blue) and trions X^- (red) from spatial locations E (**A**) and D (**C**) in the QC regime. (**B**, **D**) The corresponding peak ratios $I_{X^-}/(I_{X^0} + I_{X^-})$ show the relative number of trions and neutral excitons and reveal the underlying quantum plasmonic mechanisms. Inset shows the tip-sample distance control parameter *d* and the AFM image of the central part of the complex WS_2 nanoflake, with the marked locations of spots D and E separated by 60 nm. The peak ratios show two different types of behavior from the closely spaced locations, which may be switched by varying the tip-sample distance by only a few picometers.

spot D did not significantly change, but the X^0 PL intensity decreased because of the $X^0 \rightarrow X^-$ transition and tunneling, respectively. This indicates not only a substantial contribution of the $X^0 \rightarrow X^-$ transition in spot D but also a reversal of the peak ratio and a contribution of the opposite reaction in spot E, leading to the inverse $X^- \rightarrow X^0$ transition. This shows a strong dependence of the observed effects on the spatial location and sample heterogeneity and also provides new opportunities for controlling the subwavelength local photoresponse of excitons in 2D materials.

DISCUSSION

The TEQPL images revealed detailed inhomogeneous properties of the samples that correlated with topography and CPD measurements. TEQPL also revealed specific locations with different quenching behavior that could not be identified using the conventional FF PL, AFM, and KPFM techniques. Different regimes of PL imaging may be used for different purposes. Distance dependence may be classified on the basis of the results shown in Fig. 4 into four cases. First, the classical PL enhancement increases with the decrease in the tip-sample distance. Second, the saturation of the enhancement takes place due to the energy transfer between the tip and the sample and the competing PL suppression., Third, PL control in the QC regime is achieved below the vdW distance due to the $X^0 \rightarrow X^-$ transition. Fourth, the complete suppression of the TEQPL is due to the broken tip-substrate cavity and the formation of the classical conductive channels shown in Fig. 4C when $d < 240$ pm. Although the transition to quantum plasmonic trion generation increases the trion density in WS_2, the strong NF quenching mechanism suppresses the overall NF effects. Therefore, the tip-sample distance should be optimized on the basis of a specific target.

We distinguish two regimes of the tip-sample coupling, namely, the CC and QC regimes, which correspond to the tip-sample distance of $d > 1$ nm and $d < 0.35$ nm, respectively. In theory, we distinguish the classical TEPL and quantum TEQPL imaging techniques. However, in reality, both TEPL and TEQPL contribute in the quantum plasmonic regime of small tip-sample distance, where the classical NF effects of TEPL are still present and, in addition, the quantum plasmonic effects make a substantial contribution. The contribution of the TEQPL can be controlled by varying the tip-sample distance. Optical NF and FF images in fig. S3 show a small contribution of TEQPL and a large contribution of TEPL, which was achieved by varying the set point of the AFM measurement. The NF maps of neutral excitons and trions in fig. S3 (A and B, respectively) show correlated intensity distributions of the TEPL signals (the TEQPL signals show anticorrelated intensity distributions but contribute less in this measurement due to a different AFM set point). The comparison between the mostly TEQPL and mostly TEPL signals in Fig. 3 and fig. S3, respectively, shows the key differences between the classical and quantum plasmonic techniques. The classical TEPL technique provides nanoscale imaging by the plasmonic NF enhancement but does not allow the local control of the charged excitons and trions. The quantum plasmonic TEQPL technique provides new control tools in addition to imaging. This opens new possibilities for simultaneous imaging and control in the quantum regime.

MATERIALS AND METHODS

We performed AFM, KPFM, and TEQPL imaging of monolayer WS_2 in a Au-Ag tip-substrate cavity using a state-of-the-art commercial instrument (OmegaScope-R coupled to LabRAM, HORIBA Scientific). Plasmonic Ag tips have larger NF enhancement compared to the Au tips. However, Ag rapidly oxidizes in air, reducing the tip lifetime. Therefore, the Ag tips were coated with 3 to 4 nm of Au to protect from oxidation. The WS_2 samples were grown on Si/SiO_2 substrates via CVD and were transferred to the atomically flat Au substrates (Platypus).

AFM measurements were performed using a silicon tip with ~20-nm diameter. The scanning step size was 25 nm. Each scan took 3 min with a scanning rate of 1.0 Hz. TEPL imaging was based on the contact mode AFM. A 532-nm laser (400-μW power with an equivalent power density of 4×10^5 W/cm^2) was used for excitation and adjusted to focus on the tip apex by optimizing the microscope objective. Both the FF and NF PL signals were collected before and after the tip-sample contact. The TEQPL scanning step size was 50 nm, and the acquisition time per pixel was 0.5 s. The NF signals were obtained by subtracting the data with and without the tip contact. The overall background was removed, and the PL spectra were normalized for convenience. The contact mode AFM image, which was obtained during the TEQPL mapping simultaneously with the NF and FF PL maps in Fig. 3, shows the absence of any notable thermal drift (fig. S5).

The PL distance dependence was performed by keeping the tip stationary within the laser focus, lifting the sample up toward the tip using the piezo-electric control. The total displacement of the sample stage was 40 nm, but the actual tip-sample distance variation was less, as was previously described (*14*) and shown in fig. S1. The distance dependence data were collected using 200 steps and the 0.5-s acquisition time per step.

KPFM was performed using the same Au-coated Ag tip, as was used in TEQPL for measuring the relative surface CPD between the sample and the tip. KPFM scans were performed with a 25-nm step size under a 532-nm laser illumination. All experiments were performed under ambient conditions at room temperature.

Theoretical model

To understand the mechanisms of the two quantum plasmonic effects, that is, the tunneling-induced $X^0 \rightarrow X^-$ transition and PL quenching, we developed a rate equation model describing the distance dependence of the PL of neutral excitons X^0 and trions X^- by considering the ground $|g\rangle$, neutral exciton $|X^0\rangle$, and trion $|X^-\rangle$ states (fig. S9A) with N_g, N_{X^0}, and N_{X^-} populations, respectively

$$\frac{dN_g}{dt} = -s\Gamma_p(d)(N_g - N_{X^-}) - \Gamma_p(d)(N_g - N_{X^0}) + \Gamma_{X^0}N_{X^0} + \Gamma_{X^-}N_{X^-} \quad (1)$$

$$\frac{dN_{X^0}}{dt} = \Gamma_p(d)(N_g - N_{X^0}) - \Gamma_{CT}(d)(N_{X^0}) + \beta\,\Gamma_{CT}(d)(N_{X^-}) - \Gamma_{X^0}N_{X^0} \quad (2)$$

$$\frac{dN_{X^-}}{dt} = s\Gamma_p(d)(N_g - N_{X^-}) + \Gamma_{CT}(d)(N_{X^0}) - \beta\,\Gamma_{CT}(d)(N_{X^-}) - \Gamma_{X^-}N_{X^-} \quad (3)$$

where $\tau_{X0} = 1/\Gamma_{X^0}$ and $\tau_{X^-} = 1/\Gamma_{X^-}$ are the neutral exciton and trion relaxation times, respectively. The relaxation times of the neutral excitons and trions in WS_2 at room temperature were approximately set to $\tau_{X0} = \tau_{X^-} = 1$ ps (*40*). We only consider the NF excitation in describing the distance dependence because the FF excitation does not depend on the tip-sample distance that was kept below 10 nm. The NF neutral exciton pumping rate $\Gamma_p(d)$ depends on the tip-sample distance due to the tunneling-induced plasmonic field quenching. The corresponding NF trion pumping rate $s\Gamma_p(d)$ includes the parameter s to describe the ratio of the neutral exciton to trion excitation rate that was set to $s = 0.15$. Because we assume that the quantum quenching effects contribute at $d < 0.35$ nm, $\Gamma_p(d)$ is described by a piecewise function corresponding to the CC and QC regimes (*35*).

$$\Gamma_p(d) = \begin{cases} 1 - e^{-\frac{d-c}{d_p}}, & \text{for } d < 0.35; \\ B(R + d - c)^{-4}, & \text{for } d > 0.35 \end{cases} \quad (4)$$

In the QC regime of $d < 0.35$ nm, the parameter c represents the distance of the conductive contact between the tip and the sample with the complete quenching of the NF. The value $1/d_p = 0.02$ nm^{-1} describes the inverse mean tunneling distance. When $d > 0.35$ nm, the pumping rate is described by the NF tip-sample energy transfer function $(R + d - c)^{-4}$, where $R = 25$ nm is the tip apex radius and B is the smoothing parameter (*35*). The distance dependence of the tunneling-induced $X^0 \rightarrow X^-$ transition rate is given by $\Gamma_{CT}(d)$

$$\Gamma_{CT}(d) = \begin{cases} Ae^{-\frac{d-c}{d_{CT}}}, & \text{for } d < 0.35; \\ 0, & \text{for } d > 0.35 \end{cases} \quad (5)$$

where we assume $\Gamma_{CT}(d) = 0$ in the CC regime for $d > 0.35$ nm due to the low tunneling probability for the large tip-sample distance. The value $1/d_{CT}$ describes the inverse mean distance dependence of the $X^0 \rightarrow X^-$ transition rate. The ratio of d_{CT} and d_p shows the competition of the increase in trion PL due to the $X^0 \rightarrow X^-$ transition and the decrease in trion PL due to plasmonic quenching. A is a normalization parameter. The inverse $X^- \rightarrow X^0$ transition probability was set to $\beta = 0.001$. This model was used to fit the results shown in Fig. 4. For the complete quenching case, $d_{CT} = 0.1d_p$ and $c = 0.234$ nm. For the incomplete quenching case, $d_{CT} = 0.3d_p$ and $c = 0.220$ nm. Our results show that the main differences between the complete and incomplete quenching are the larger parameters $1/d_{CT}$ and c in the case of the complete quenching, which shows the rapid increase in the $X^0 \rightarrow X^-$ transition rate with the decrease in the tip-sample distance d. Incomplete quenching shows the slow increase in the $X^0 \rightarrow X^-$ transition rate with d, which cannot reach a notable value before the quantum quenching suppresses the NF PL.

SUPPLEMENTARY MATERIALS

Supplementary material for this article is available at http://advances.sciencemag.org/cgi/content/full/5/10/eaau8763/DC1

Fig. S1. AFM force-distance diagram.
Fig. S2. Tip-sample distance dependence of the neutral exciton/trion PL.
Fig. S3. Classical TEPL imaging.
Fig. S4. Kelvin probe force microscopy.
Fig. S5. AFM obtained during TEQPL imaging.
Fig. S6. Repeated distance dependence measurements of spot B.
Fig. S7. Anticorrelated distributions of neutral excitons and trions under TEQPL.
Fig. S8. Mixed distributions of neutral excitons and trions.
Fig. S9. The model and simulation of TEQPL.
Fig. S10. PL and peak assignment of WS_2 on Si/SiO_2.

REFERENCES AND NOTES

1. K. F. Mak, J. Shan, Photonics and optoelectronics of 2D semiconductor transition metal dichalcogenides. *Nat. Photonics* **10**, 216–226 (2016).
2. R. Lv, J. A. Robinson, R. E. Schaak, D. Sun, Y. Sun, T. E. Mallouk, M. Terrones, Transition metal dichalcogenides and beyond: Synthesis, properties, and applications of single- and few-layer nanosheets. *Acc. Chem. Res.* **48**, 56–64 (2014).

3. S. Z. Butler, S. M. Hollen, L. Cao, Y. Cui, J. A. Gupta, H. R. Gutiérrez, T. F. Heinz, S. S. Hong, J. Huang, A. F. Ismach, E. Johnston-Halperin, M. Kuno, V. V. Plashnitsa, R. D. Robinson, R. S. Ruoff, S. Salahuddin, J. Shan, L. Shi, M. G. Spencer, M. Terrones, W. Windl, J. E. Goldberger, Progress, challenges, and opportunities in two-dimensional materials beyond graphene. *ACS Nano* **7**, 2898–2926 (2013).
4. A. Boulesbaa, B. Huang, K. Wang, M.-W. Lin, M. Mahjouri-Samani, C. Rouleau, K. Xiao, M. Yoon, B. Sumpter, A. Puretzky, D. Geohegan, Observation of two distinct negative trions in tungsten disulfide monolayers. *Phys. Rev. B* **92**, 115443 (2015).
5. Y. You, X.-X. Zhang, T. C. Berkelbach, M. S. Hybertsen, D. R. Reichman, T. F. Heinz, Observation of biexcitons in monolayer WSe_2. *Nat. Phys.* **11**, 477–481 (2015).
6. A. Singh, G. Moody, K. Tran, M. E. Scott, V. Overbeck, G. Berghäuser, J. Schaibley, E. J. Seifert, D. Pleskot, N. M. Gabor, J. Yan, D. G. Mandrus, M. Richter, E. Malic, X. Xu, X. Li, Trion formation dynamics in monolayer transition metal dichalcogenides. *Phys. Rev. B* **93**, 041401 (2016).
7. M. Yoshida, A. Popert, Y. K. Kato, Gate-voltage induced trions in suspended carbon nanotubes. *Phys. Rev. B* **93**, 041402 (2016).
8. A. A. Mitioglu, P. Plochocka, J. N. Jadczak, W. Escoffier, G. L. J. A. Rikken, L. Kulyuk, D. K. Maude, Optical manipulation of the exciton charge state in single-layer tungsten disulfide. *Phys. Rev. B* **88**, 245403 (2013).
9. J. Li, Q. Ji, S. Chu, Y. Zhang, Y. Li, Q. Gong, K. Liu, K. Shi, Tuning the photo-response in monolayer MoS2 by plasmonic nano-antenna |. *Sci. Rep.* **6**, 23626 (2016).
10. N. Peimyoo, W. Yang, J. Shang, X. Shen, Y. Wang, T. Yu, Chemically driven tunable light emission of charged and neutral excitons in monolayer WS_2. *ACS Nano* **8**, 11320–11329 (2014).
11. S. Liang, Z. Ma, N. Wei, H. Liu, S. Wang, L.-M. Peng, Solid state carbon nanotube device for controllable trion electroluminescence emission. *Nanoscale* **8**, 6761–6769 (2016).
12. K. F. Mak, K. He, C. Lee, G. H. Lee, J. Hone, T. F. Heinz, J. Shan, Tightly bound trions in monolayer MoS_2. *Nat. Mater.* **12**, 207–211 (2013).
13. M. S. Tame, K. R. McEnery, Ş. K. Özdemir, J. Lee, S. A. Maier, M. S. Kim, Quantum plasmonics. *Nat. Phys.* **9**, 329–340 (2013).
14. Y. Zhang, D. V. Voronine, S. Qiu, A. M. Sinyukov, M. Hamilton, Z. Liege, A. V. Sokolov, Z. Zhang, M. O. Scully, Improving resolution in quantum subnanometre-gap tip-enhanced Raman nanoimaging. *Sci. Rep.* **6**, 25788 (2016).
15. X. Yang, H. Yu, X. Guo, Q. Ding, T. Pullerits, R. Wang, G. Zhang, W. Liang, M. Sun, Plasmon-exciton coupling of monolayer MoS_2-Ag nanoparticles hybrids for surface catalytic reaction. *Mater. Today Energy* **5**, 72–78 (2017).
16. S. Najmaei, A. Mlayah, A. Arbouet, C. Girard, J. Léotin, J. Lou, Plasmonic pumping of excitonic photoluminescence in hybrid MoS_2–Au nanostructures. *ACS Nano* **8**, 12682–12689 (2014).
17. W. Su, N. Kumar, S. Mignuzzi, J. Crain, D. Roy, Nanoscale mapping of excitonic processes in single-layer MoS_2 using tip-enhanced photoluminescence microscopy. *Nanoscale* **8**, 10564–10569 (2016).
18. W. Zhu, R. Esteban, A. G. Borisov, J. J. Baumberg, P. Nordlander, H. J. Lezec, J. Aizpurua, K. B. Crozier, Quantum mechanical effects in plasmonic structures with subnanometre gaps. *Nat. Commun.* **7**, 11495 (2016).
19. Y. Wang, C. Cong, W. Yang, J. Shang, N. Peimyoo, Y. Chen, J. Kang, J. Wang, W. Huang, T. Yu, Strain-induced direct–indirect bandgap transition and phonon modulation in monolayer WS_2. *Nano Res.* **8**, 2562–2572 (2015).
20. A. Bondi, van der Waals volumes and radii. *J. Phys. Chem.* **68**, 441–451 (1964).
21. S. J. Yun, S. H. Chae, H. Kim, J. C. Park, J.-H. Park, G. H. Han, J. S. Lee, S. M. Kim, H. M. Oh, J. Seok, M. S. Jeong, K. K. Kim, Y. H. Lee, Synthesis of centimeter-scale monolayer tungsten disulfide film on gold foils. *ACS Nano* **9**, 5510–5519 (2015).
22. K. Wei, Y. Liu, H. Yang, X. Cheng, T. Jiang, Large range modification of exciton species in monolayer WS_2. *Appl. Opt.* **55**, 6251–6255 (2016).
23. T. Kato, T. Kaneko, Transport dynamics of neutral excitons and trions in monolayer WS_2. *ACS Nano* **10**, 9687–9694 (2016).
24. S. Matthews, C. Zhao, H. Zeng, F. V. Bright, effects of acetone vapor on the exciton band photoluminescence emission from single- and few-layer WS_2 on template-stripped gold. *Sensors* **19**, E1913 (2019).
25. Y. Zeng, W. Chen, B. Tang, J. Liao, J. Lou, Q. Chen, Synergetic photoluminescence enhancement of monolayer MoS_2 via surface plasmon resonance and defect repair. *RSC Adv.* **8**, 23591–23598 (2018).
26. Y. Zeng, X. Li, W. Chen, J. Liao, J. Lou, Q. Chen, Highly enhanced photoluminescence of monolayer MoS_2 with self-assembled Au nanoparticle arrays. *Adv. Mater. Interfaces* **4**, 1700739 (2017).
27. Z. Wu, N. Zhu, J. Jiang, A. Zafar, J. Hong, Y. Zhang, Tuning interlayer coupling by laser irradiation and broadband photodetection in vertical $MoTe_2/WS_2$ vdW heterostructure. *APL Materials* **7**, 041108 (2019).
28. Y. Kwon, K. Kim, W. Kim, S. Ryu, H. Cheong, Variation of photoluminescence spectral line shape of monolayer WS_2. *Curr. Appl. Phys.* **18**, 941–945 (2018).
29. M. Drüppel, T. Deilmann, P. Krüger, M. Rohlfing, Diversity of trion states and substrate effects in the optical properties of an MoS_2 monolayer. *Nat. Commun.* **8**, 2117 (2017).
30. T. C. Berkelbach, M. S. Hybertsen, D. R. Reichman, Theory of neutral and charged excitons in monolayer transition metal dichalcogenides. *Phys. Rev. B* **88**, 045318 (2013).
31. A. Chernikov, T. C. Berkelbach, H. M. Hill, A. Rigosi, Y. Li, O. B. Aslan, D. R. Reichman, M. S. Hybertsen, T. F. Heinz, Exciton binding energy and nonhydrogenic Rydberg series in monolayer WS_2. *Phys. Rev. Lett.* **113**, 076802 (2014).
32. E. Courtade, M. Semina, M. Manca, M. M. Glazov, C. Robert, F. Cadiz, G. Wang, T. Taniguchi, K. Watanabe, M. Pierre, W. Escoffier, E. L. Ivchenko, P. Renucci, X. Marie, T. Amand, B. Urbaszek, Charged excitons in monolayer WSe_2: Experiment and theory. *Phys. Rev. B* **96**, 085302 (2017).
33. S. Borghardt, J.-S. Tu, F. Winkler, J. Schubert, W. Zander, K. Leosson, B. E. Kardynał, Engineering of optical and electronic band gaps in transition metal dichalcogenide monolayers through external dielectric *screening*. *Phys. Rev. Mater.* **1**, 054001 (2017).
34. D. Van Tuan, M. Yang, H. Dery, Coulomb interaction in monolayer transition-metal dichalcogenides. *Phys. Rev. B* **98**, 125308 (2018).
35. K.-D. Park, O. Khatib, V. Kravtsov, G. Clark, X. Xu, M. B. Raschke, Hybrid tip-enhanced nanospectroscopy and nanoimaging of monolayer WSe_2 with local strain control. *Nano Lett.* **16**, 2621–2627 (2016).
36. X. Wang, D. Zhang, K. Braun, H. J. Egelhaaf, C. J. Brabec, A. J. Meixner, High-resolution spectroscopic mapping of the chemical contrast from nanometer domains in P3HT:PCBM organic blend films for solar-cell applications. *Adv. Funct. Mater.* **20**, 492–499 (2010).
37. D. V. Voronine, G. Lu, D. Zhu, A. Krayev, Tip-enhanced Raman scattering of MoS_2. *IEEE J. Sel. Top. Quantum Electron.* **23**, 138–143 (2017).
38. R. T. Tung, The physics and chemistry of the Schottky barrier height. *Appl. Phys. Rev.* **1**, 011304 (2014).
39. J. Zuloaga, E. Prodan, P. Nordlander, Quantum description of the plasmon resonances of a nanoparticle dimer. *Nano Lett.* **9**, 887–891 (2009).
40. Y. Yu, S. Hu, L. Su, L. Huang, Y. Liu, Z. Jin, A. A. Purezky, D. B. Geohegan, K. W. Kim, Y. Zhang, L. Cao, Equally efficient interlayer exciton relaxation and improved absorption in epitaxial and nonepitaxial MoS_2/WS_2 heterostructures. *Nano Lett.* **15**, 486–491 (2014).

Acknowledgments: We thank Y. Zhang for helpful discussions. We thank S. Ambardar for help with data processing and for helpful discussions. **Funding:** This work was supported by the Office of Naval Research (grant no. N00014-16-1-3054), the Robert A. Welch Foundation (Grant no. A1261), Air Force Office of Scientific Research (award no. FA9550-18-1-0141), and NSF (grant nos. CHE-1609608, ECCS 1809622 and IIP-1539999). Z. He was supported by the Herman F. Heep and Minnie Belle Heep Texas A&M University Endowed Fund held/administered by the Texas A&M Foundation. **Author contributions:** Z. He, D.V.V. and M.O.S conceived the experiments and/or developed the laboratory. Z. He, Z. Han, and D.V.V. performed the tip-enhanced Raman scattering experiments. Z. He, H.E., C.N., J.H., and D.V.V. developed the model and simulations. J.Y. and J.L. produced the WS_2 samples. Z. He, Z. Han, and A.M.S. did the spectroscopy analysis. Z. He, Z.Z., J.H., D.V.V., and M.O.S. discussed and wrote the manuscript. All authors contributed to the experiments and manuscript preparation. **Competing interests:** The authors declare that they have no competing interests. **Data and materials availability:** All data needed to evaluate the conclusions in the paper are present in the paper and/or the Supplementary Materials. The datasets generated and/or analyzed during the current study are available from D.V.V. (voronine@usf.edu) or Z.H. (hezhe@physics.tamu.edu) on reasonable request.

Submitted 24 July 2018
Accepted 14 September 2019
Published 11 October 2019
10.1126/sciadv.aau8763

Citation: Z. He, Z. Han, J. Yuan, A. M. Sinyukov, H. Eleuch, C. Niu, Z. Zhang, J. Lou, J. Hu, D. V. Voronine, M. O. Scully, Quantum plasmonic control of trions in a picocavity with monolayer WS_2. *Sci. Adv.* **5**, eaau8763 (2019).

Science Advances

Quantum plasmonic control of trions in a picocavity with monolayer WS_2

Zhe He, Zehua Han, Jiangtan Yuan, Alexander M. Sinyukov, Hichem Eleuch, Chao Niu, Zhenrong Zhang, Jun Lou, Jonathan Hu, Dmitri V. Voronine and Marlan O. Scully

Sci Adv **5** (10), eaau8763.
DOI: 10.1126/sciadv.aau8763

Science Advances (ISSN 2375-2548) is published by the American Association for the Advancement of Science, 1200 New York Avenue NW, Washington, DC 20005. The title *Science Advances* is a registered trademark of AAAS.